*Article*

# LaNi$_{0.6}$Co$_{0.4-x}$Fe$_x$O$_{3-\delta}$ as Air-Side Contact Material for La$_{0.3}$Ca$_{0.7}$Fe$_{0.7}$Cr$_{0.3}$O$_{3-\delta}$ Reversible Solid Oxide Fuel Cell Electrodes

Kalpana Singh [1], Paul Kwesi Addo [1], Venkataraman Thangadurai [2], Jesús Prado-Gonjal [3] and Beatriz Molero-Sánchez [1,*]

[1] SeeO2 Energy, 3655 36 St NW, Calgary, AB T2L 1Y8, Canada; ksingh@seeo2energy.com (K.S.); pkaddo@seeo2energy.com (P.K.A.)
[2] Department of Chemistry, University of Calgary, Calgary, AB T2N 1N4, Canada; vthangad@ucalgary.ca
[3] Departamento de Química Inorgánica, Facultad de Ciencias Químicas, Universidad Complutense de Madrid, 28040 Madrid, Spain; jpradogo@ucm.es
* Correspondence: bmoleros@seeo2energy.com; Tel.: +1-403-510-2505

**Abstract:** The goal of the current work was to identify an air-side-optimized contact material for La$_{0.3}$Ca$_{0.7}$Fe$_{0.7}$Cr$_{0.3}$O$_{3-\delta}$ (LCFCr) electrodes and a Crofer22APU interconnect for use in reversible solid oxide fuel cells (RSOFCs). LaNi$_{0.6}$Co$_{0.4-x}$Fe$_x$O$_3$ (x = 0–0.3) perovskite-type oxides were investigated in this work. The partial substitution of Co by Fe decreased the thermal expansion coefficient values (TEC) closer to the values of the LCFCr and Crofer 22 APU interconnects. The oxides were synthesized using the glycine–nitrate method and were characterized using X-ray thermodiffraction and 4-probe DC electrical conductivity measurements. Based on the materials characterization results from the Fe-doped oxides investigated here, the LaNi$_{0.6}$Co$_{0.2}$Fe$_{0.2}$O$_{3-\delta}$ composition was selected as a good candidate for the contact material, as it exhibited an acceptable electrical conductivity value of 395 S·cm$^{-1}$ at 800 °C in air and a TEC value of 14.98 × 10$^{-6}$ K$^{-1}$ (RT-900 °C).

## 1. Introduction

Reversible solid oxide fuel cells (RSOFCs) are green, flexible, and efficient electrochemical devices that function efficiently under both fuel cell and electrolysis modes [1]. In the fuel cell mode, RSOFCs generate clean power by electrochemically converting fuels (H$_2$, hydrocarbons, alcohols, etc.) with O$_2$ from air and function as solid oxide fuel cells (SOFCs); in the electrolysis mode, RSOFCs generate H$_2$ or useful chemicals by utilising excess renewable electricity and function as solid oxide electrolysis cells (SOECs) [1–4].

To scale up the technology and to obtain higher fuel or energy production or currents, RSOFC stacks are made by connecting several cells in series using metal interconnects. Resistance loss of the stack arising due to poor interfacial contact between the electrode and the interconnect is reduced through the use of contact materials. Contact materials are applied between electrodes and interconnects to reduce the interfacial resistance by providing a high electrical conduction path. Noble metals (Ag, Pt, Au, and Cu), Ag-containing Ni alloys, oxides (CuO), noble metal–perovskite composites (Ag-(La$_{0.6}$Sr$_{0.4}$)(Co$_{0.8}$Fe$_{0.2}$)O$_3$, Ag-La$_{0.8}$Sr$_{0.2}$MnO$_3$), perovskites (La$_{0.8}$Sr$_{0.2}$Co$_{0.75}$Fe$_{0.25}$O$_3$, La$_{0.8}$Sr$_{0.2}$FeO$_3$, LaNi$_{0.6}$Fe$_{0.4}$O$_3$, La$_{0.8}$Sr$_{0.2}$FeO$_3$, LaNi$_{0.6}$Fe$_{0.4}$O$_3$, Sm$_{0.5}$Sr$_{0.5}$CoO$_3$, La$_{0.65}$Sr$_{0.3}$MnO$_3$, Sm$_{0.5}$Sr$_{0.5}$CoO$_3$, La$_{0.7}$Sr$_{0.3}$CoO$_3$), spinels (M$_3$O$_4$, M = Ni, Mn, Co, Cu, Fe), and Ni$_{0.33}$Co$_{0.67}$O oxides have been tested in the literature as contact materials [5–8].

The electrical contacts between electrodes and interconnects have been improved in previous studies, with contact materials showing chemical reactivity with Cr-containing

interconnects and formed secondary phases of $Ag_2CrO_4$, $AgCrO_2$, $SrCrO_4$, Cr-spinels, or Cr-perovskites [9–11]. Additionally, the reports are scarce on the effects of different types of contact materials and degradation mechanisms on the performance of the RSOFCs stacks in the electrolyzer mode [12,13].

In recent years, $La_{0.3}Ca_{0.7}Fe_{0.7}Cr_{0.3}O_{3-\delta}$ (LCFCr) has exhibited excellent properties as an electrocatalyst for RSOFC systems [14–22]. Owing to its stable and highly active electrochemical performance in fuel ($CO_2$/CO/steam) and oxygen environments, LCFCr can be used as both the fuel and for oxygen electrodes. Contact materials are crucial components in terms of the technology scale-up, stack manufacturing, and long-term electrochemical performance.

The following properties need to be fulfilled for materials to be considered as good candidates for contact materials: high electrical conductivity, matching thermal expansion properties with the other cell components, and appropriate sintering activity. Low electrical conductivity of the contact material results in high total interfacial ohmic resistance, leading to lower electrochemical performance. Mismatched thermal expansion properties result in delamination, deformation, or even cell fracture during thermal cycling [7]. Limited sintering activity leads to weak adherence of the contact material with the adjacent electrodes and interconnects [11]. Additional desired material properties include chemical compatibility with the interconnects and the electrodes and no undesirable reactions leading to low conducting phases or poor thermal expansion coefficient matches. If there are side reactions, then the resultant phases should possess high electrical conductivity, appropriate thermal expansion, high thermochemical activity, and structural stability in oxidizing and reducing environments.

In the present work, air-side contact materials for RSOFCs were investigated for LCFCr electrodes. Conventionally used contact materials include Au and other expensive precious metals [10,23]. Although Ag and Ag-containing Ni alloys are more economical than other noble metals, the rapid thermal etching required and their high volatility at high temperatures limit their applications as contact materials [24–26]. Hence, researchers have been investigating perovskite-type oxides as possible contact materials. $LaNi_{0.6}Co_{0.4}O_{3-\delta}$ has been tested by various researchers as a contact material owing to its high electrical conductivity; however, its thermal expansion coefficient (TEC) values are high (up to $17.5 \times 10^{-6}$ $K^{-1}$) when compared to the TEC values of the LCFCr electrocatalyst ($11.75 \times 10^{-6}$ $K^{-1}$) [14,27,28].

The Crofer 22 APU/$LaNi_{0.6}Co_{0.4}O_{3-\delta}$/$La_{0.6}Sr_{0.4}FeO_3$ assembly showed the lowest area-specific resistance (ASR) value owing to the high electrical conductivity of $LaNi_{0.6}Co_{0.4}O_{3-\delta}$ when compared to assemblies with $(La_{0.8}Sr_{0.2})_{0.95}Fe_{0.6}Mn_{0.3}Co_{0.1}O_3$ and $LaNi_{0.6}Fe_{0.4}O_{3-\delta}$ as contact materials [27]. As stated earlier, the TEC values of $LaNi_{0.6}Co_{0.4}O_{3-\delta}$ are high, and in order to be used as contact materials, a doping approach must be employed to bring down the TEC values. It has been shown in the literature that substituting Co by Fe can significantly reduce the TEC values. For example, the TEC values of $Ln_{1-x}Sr_xCo_{1-y}Fe_yO_{3-\delta}$ (Ln = Pr, Nd, Gd; x = 0.2, 0.3; $0 \leqq y \leqq 1$), $PrBaCo_{2-x}Fe_xO_{5+\delta}$ (x = 0, 0.5, 1.0, 1.5 and 2.0), $PrBa_{0.5}Sr_{0.5}Co_{2-x}Fe_xO_{5+\delta}$ (x = 0, 0.5 and 1.0), and $La_{0.8}Sr_{0.2}Co_{1-x}Fe_xO_{3-\delta}$ (x = 0.2, 0.5, 0.8) decreased with increasing Fe content [29–32]. Substituting Fe for Co sites lowers the relative spin-state transition of $Co^{3+}$ ions from low to high spin states by decreasing the Co content. Hence, in the proposed research, $LaNi_{0.6}Co_{0.4}O_{3-\delta}$ was doped with Fe to make $LaNi_{0.6}Co_{0.4-x}Fe_xO_{3-\delta}$ (x = 0–0.3) composites, with the aim of reducing the TEC values while still maintaining acceptable electrical conductivity values at an operating temperature of 800 °C. In the present work, Crofer 22 APU was chosen as the interconnect as it is commercially used, exhibits a low oxidation rate, and adheres properly to oxide electrodes by forming highly conductive oxide scales [33].

$LaNi_{0.6}Co_{0.4-x}Fe_xO_{3-\delta}$ (x = 0–0.3) oxides were screened as air-side contact materials based on the electrical conductivity, TEC values, and chemical compatibility with Crofer 22 APU and LCFCr.

## 2. Materials and Methods

LaNi$_{0.6}$Co$_{0.4-x}$Fe$_x$O$_{3-\delta}$ (x = 0–0.3) synthesis: Stoichiometric amounts of La(NO$_3$)$_2$·6H$_2$O, Ni(NO$_3$)$_2$.6H$_2$O, Co(NO$_3$)$_2$·6H$_2$O, and Fe(NO$_3$)$_3$·9H$_2$O were first dissolved in deionized water, then the stoichiometric amount of glycine was added to the metal nitrate solution to prepare the desired compositions. The molar ratio of glycine to the total content of the nitrates was 2:1. All chemicals were bought from Alfa Aesar (Ward Hill, MA, USA) with purity > 98.5%. The solution was stirred thoroughly and heated on a hot plate at 300–350 °C until self-combustion occurred. The powders were grounded and calcined to produce single-phase powders. Table 1 shows the respective calcination temperature and duration needed to achieve crystalline and pure phases. A heating and cooling rate of 5°/min was used to prepare all samples.

**Table 1.** Calcination temperature (CT) used for preparing single-phase powders of LaNi$_{0.6}$Co$_{0.4-x}$Fe$_x$O$_{3-\delta}$ (x = 0.1, 0.2, 0.3) and sintering temperature (ST) used for the fabrication of cylindrical pellets for conductivity measurements, along with the relative density values measured using the Archimedes method.

| Composition | CT (°C)/ Time (h) | ST (°C)/Time (h) | Relative Density of Pellets (%) |
|---|---|---|---|
| LaNi$_{0.6}$Co$_{0.4}$O$_{3-\delta}$ | 800/5 | 1300/5 | ~97 |
| LaNi$_{0.6}$Co$_{0.3}$Fe$_{0.1}$O$_{3-\delta}$ | 1000/5 | 1300/5 | ~95 |
| LaNi$_{0.6}$Co$_{0.2}$Fe$_{0.2}$O$_{3-\delta}$ | 1000/5 | 1300/5 | ~93 |
| LaNi$_{0.6}$Co$_{0.1}$Fe$_{0.3}$O$_{3-\delta}$ | 1000/5 | – | ~93 |

La$_{0.3}$Ca$_{0.7}$Fe$_{0.7}$Cr$_{0.3}$O$_{3-\delta}$ synthesis: Stoichiometric amounts of La(NO$_3$)$_2$·6H$_2$O, Ca(NO$_3$)$_2$ 4H$_2$O, Fe(NO$_3$)$_3$·9H$_2$O, and Cr(NO$_3$)$_3$·9H$_2$O were dissolved in deionized water. A stoichiometric amount of glycine (2:1 molar ratio to cations) was added to the metal nitrate solution. All chemicals were purchased from Alfa Aesar (Ward Hill, MA, USA) with purity > 98.5 %. The solution was slowly stirred on a hot plate until gel formed, leading to auto-ignition and self-sustaining combustion. The powders were first ground in a mortar and pestle and then calcined in air at 1200 °C for 2 h (heating and cooling rate of 5°/min) to obtain a single phase [14,15,20].

Interconnect: Crofer22 APU ferritic stainless steel developed by Forschungszentrum Julich and commercialized by ThyssenKrupp VDM (Werdohl, Germany) was used as the interconnect [34]. The nominal composition of Crofer 22 APU listed by ThyssenKrupp VDM (Werdohl, Germany) in wt.% is as follows: 20–24 Cr, 0.3–0.8 Mn, 0.03–0.2 Ti, 0.04–0.2 La, 0.003 C, 0.05 P, 0.020 S, balance Fe [35].

Phase analysis: Room temperature powder X-ray diffraction (PXRD) patterns of all samples were collected using a Bruker D8 Advance X-ray diffractometer (Karlsruhe, Germany) with Cu K$\alpha$ monochromatic radiation ($\lambda$ = 1.54056 Å), operating at 45 kV and 40 mA. XRD patterns were collected in the 2$\theta$ range of 10–80° at room temperature with a step size of 0.03° and a 10 second counting time. X-ray thermodiffraction patterns were collected on an PANalytical X'Pert PRO MPD diffractometer (Malvern, UK) with a high-temperature reactor chamber and Anton Paar HTK1200 camera with Cu K$\alpha$ monochromatic radiation ($\lambda$ = 1.54056 Å). The data were collected in the 2$\theta$ range of 10–80° with an angle step size of 0.03° and a 25 s counting time. The sample was heated to the target temperatures (RT to 1100 °C) at a ramp rate of 5° C/min. Before the measurements, samples were stabilized in the air for 40 min. The conventional Rietveld method using the General Structure Analysis System (GSAS) package with graphical user interface (EXPGUI) software was employed to calculate lattice parameters through the Le Bail fit and to refine the X-ray diffraction patterns. The relative density of sintered pellets was calculated as the experimental density/theoretical density. The experimental density or bulk density of sintered pellets was measured by Archimedes method and the theoretical density was obtained from the Rietveld refinement of XRD data. The average lattice thermal expansion

($\alpha$) values of as-prepared powders were calculated from the line of best fit of the graph (($\Delta L/L_0$ vs. temperature)) (Equation (1)):

$$a_{T-To} = \left(\frac{\Delta L}{L_o}\right)\left(\frac{1}{T - T_o}\right) \tag{1}$$

where $\Delta L/L_0$ is the ratio between the relative changes in the lattice parameter (($a - a_0)/a_0$) at a specific temperature ($T$) compared with its value at room temperature ($T_0$). At room temperature, it was assumed that no lattice expansion occurred.

Chemical compatibility: The reactivity between the contact material and LCFCr powders was analyzed by mixing powders at weight ratios of 30:70 and 50:50 and by heating the powders at 800 °C for 120 h in air and analyzing the mixed phases through XRD. The reactivity between the Crofer 22 APU/contact material assembly was analyzed by first screen painting contact materials over oxidized Crofer 22 APU interconnect, and then heating the assembly at 800 °C for 120 h in air. The assembly were analyzed through XRD to assess the possible formation of any secondary phases after heat treatment.

Electrical conductivity: For bulk electrical conductivity measurements, cylindrical pellets of as-prepared powders were sintered at 1300 °C for 5 h to attain the highest density (Table 1). The bulk electrical conductivity measurements of contact materials were carried out by direct current (DC) four-point method from room temperature to 800 °C in air by employing Biologic VSP-300 (Seyssinet-Pariset, France) Potentiostat.

## 3. Results and Discussion

PXRD patterns for $LaNi_{0.6}Co_{0.4-x}Fe_xO_{3-\delta}$ (x = 0–0.3) series are shown in Figure 1a–c, where Figure 1c shows the Rietveld X-ray diffraction pattern refinement for $LaNi_{0.6}Co_{0.4-x}Fe_xO_{3-\delta}$ as an example. $LaNi_{0.6}Co_{0.4}O_{3-\delta}$ was indexed with a rhombohedral crystal structure assigned to the *R-3c* space group (#167). The rhombohedral phase is retained after Fe doping along with changes in lattice parameters (Table 2). The $LaNi_{0.6}Co_{0.1}Fe_{0.3}O_{3-\delta}$ composition showed the presence of impurity peaks related to $Fe_3O_4$. Fe doping led to the shift in diffraction peaks to lower diffraction angles, indicating an increase in the lattice constant, as the ionic radius of $Fe^{3+}$ (0.55/0.645 Å (LS/HS) is slightly larger than the ionic radii of $Co^{3+}$ 0.545/0.61 (LS/HS) in six-fold coordination [36]. Due to the presence of $Fe_3O_4$ impurities, the $LaNi_{0.6}Co_{0.1}Fe_{0.3}O_{3-\delta}$ composition was not further investigated as a possible candidate for a contact material.
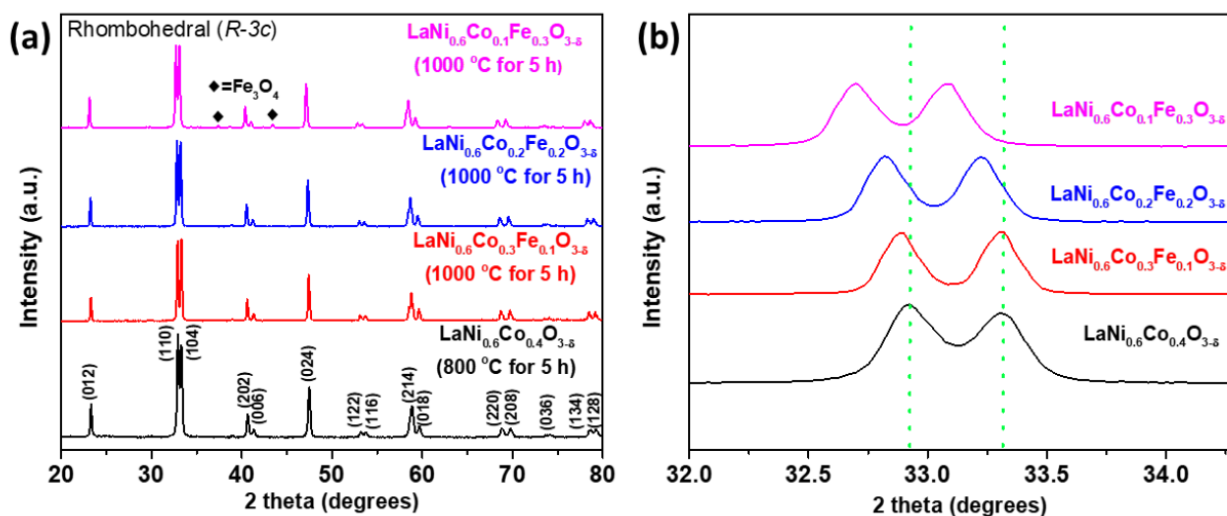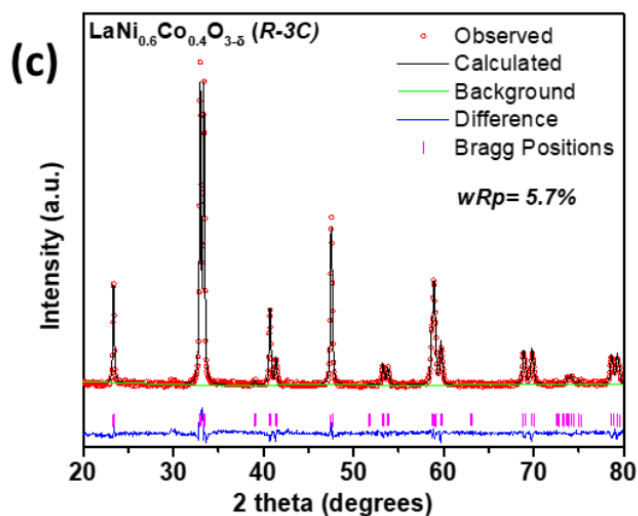


**Figure 1.** *Cont.*

**Figure 1.** Room temperature PXRD patterns of (**a**) as-prepared $LaNi_{0.6}Co_{0.4-x}Fe_xO_{3-\delta}$ (x = 0, 0.1, 0.2, 0.3) powders. (**b**) Magnified PXRD patterns in the 2-theta range of 32–34 showing the shift in peaks towards lower 2-theta degrees. (**c**) Rietveld X-ray diffraction pattern refinements for $LaNi_{0.6}Co_{0.4-x}Fe_xO_{3-\delta}$ powders: observed (red), calculated (black), background (green), and difference (blue) profiles.

**Table 2.** Lattice parameters and electrical conductivity values of $LaNi_{0.6}Co_{0.4-x}Fe_xO_{3-\delta}$ (x = 0, 0.1, 0.2, 0.3) pellets sintered at 1300 °C.

| Composition | Lattice Parameters | | $\sigma_{(800\,°C)}$ (S·cm$^{-1}$) |
|---|---|---|---|
| | a, b (Å) | c (Å) | |
| $LaNi_{0.6}Co_{0.4}O_{3-\delta}$ | 5.4681 (3) | 13.1622 (9) | ~369 |
| $LaNi_{0.6}Co_{0.3}Fe_{0.1}O_{3-\delta}$ | 5.4729 (1) | 13.1614 (5) | ~697 |
| $LaNi_{0.6}Co_{0.2}Fe_{0.2}O_{3-\delta}$ | 5.4827 (3) | 13.1937 (6) | ~395 |
| $LaNi_{0.6}Co_{0.1}Fe_{0.3}O_{3-\delta}$ | 5.4935 (3) | 13.2282 (7) | – |

Figure 2 shows the PXRD patterns for mixtures of $LaNi_{0.6}Co_{0.4-x}Fe_xO_{3-\delta}$ (x = 0, 0.1, 0.2) powders with LCFCr (in 30:70 and 50:50 wt. ratios) powders after heat treatment at 800 °C for 120 h. As shown in Figure 2, there is no indication of any new phases forming after heat treatment in any composition, indicating good chemical compatibility between the electrode material and the proposed contact compositions. However, the presence of $Cr_2O_3$ peaks in samples arising from LCFCr oxidation can be seen.

Figure 3 shows the XRD patterns on the oxidized Crofer 22 APU/$LaNi_{0.6}Co_{0.4}O_{3-\delta}$ assembly after heat treatment for 120 h at 800 °C. It can be seen that no additional peaks were detected when compared to as-prepared phase of $LaNi_{0.6}Co_{0.4}O_{3-\delta}$. Peaks attributed to the oxidized Crofer 22 APU interconnect materials can be seen, indicating that X-rays were able to penetrate through the $LaNi_{0.6}Co_{0.4}O_{3-\delta}$ layer. The reactivity studies on the oxidized Crofer 22 APU/$LaNi_{0.6}Co_{0.4}O_{3-\delta}$ assembly are shown as a representative example, as $LaNi_{0.6}Co_{0.4}O_{3-\delta}$ is the parent phase. Similar results were also seen for x = 0.1 and 0.2 compositions.

Figure 4 shows the thermodiffraction patterns for $LaNi_{0.6}Co_{0.2}Fe_{0.2}O_{3-\delta}$ in air from room temperature to 1100 °C. Thermodiffraction measurements were performed on the x = 0.2 composition to see how much the TEC value decreased for the single-phase composition with the highest Fe substitution when compared to the literature value of $LaNi_{0.6}Co_{0.4}O_{3-\delta}$. The rhombohedral perovskite phase was maintained until 900 °C, after which orthorhombic distortion was seen. The magnified PXRD patterns from 31 to 35 2-theta degrees show a shift in the peak positions towards lower 2-theta degrees, indicating an increase

in lattice parameters due to chemical expansion resulting from the reduction of cations (Equation (2)).
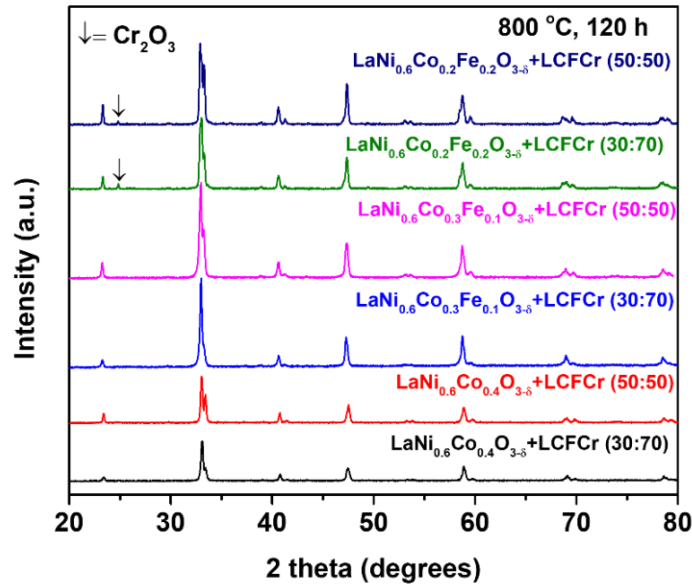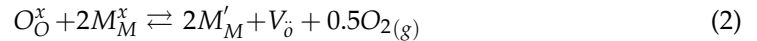
$$O_O^x + 2M_M^x \rightleftarrows 2M_M' + V_{\ddot{o}} + 0.5O_{2(g)} \tag{2}$$



**Figure 2.** Room temperature PXRD patterns for the mixture of $LaNi_{0.6}Co_{0.4-x}Fe_xO_{3-\delta}$ (x = 0, 0.1, 0.2) with LCFCr powders after heat treatment at 800 °C for 120 h in air.



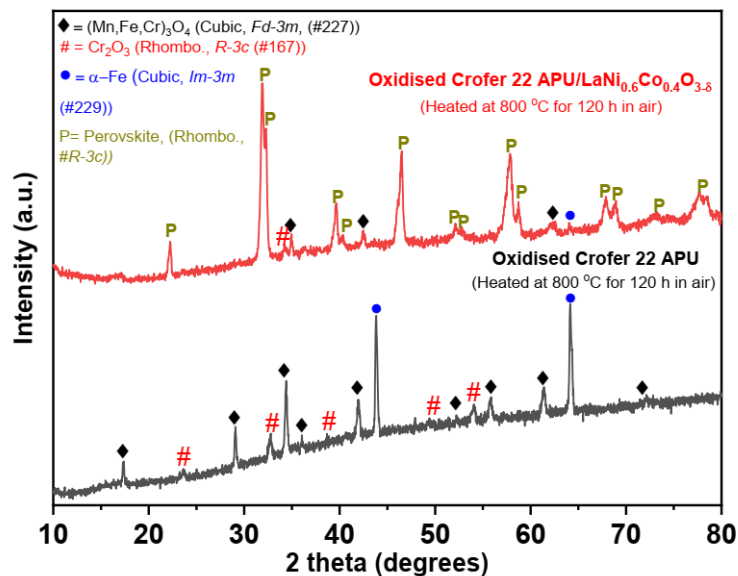**Figure 3.** Room temperature XRD patterns of oxidized Crofer22 APU coupon (black) and oxidized Crofer 22 APU/$LaNi_{0.6}Co_{0.4}O_{3-\delta}$ assembly (red) after heat treatment at 800 °C in air for 120 h.

The apparent thermal expansion ($\alpha_{ap}$) for the oxides is caused by both the chemical expansion and the thermal expansion. The chemical expansion is dependent on the changes in concentration of oxide ion vacancies ($V_{\ddot{o}}$) and is affected by two competing mechanisms: (i) the lattice expansion due to the thermal and chemical reduction of redox active cations such as Ni, Co, and Fe to lower oxidation states with larger ionic radii (Equation (2)); (ii) the lattice contraction due the electrostatic repulsion of the cations surrounding the positively charged oxide ion vacancies ($V_{\ddot{o}}$). On the other hand, thermal expansion originates from the anharmonicity of the lattice vibrations and is dependent on the electrostatic attraction forces within the lattice. The concentrations of positive and

negative charges and their distances within the lattice influence the electrostatic attraction forces [32,37–39].
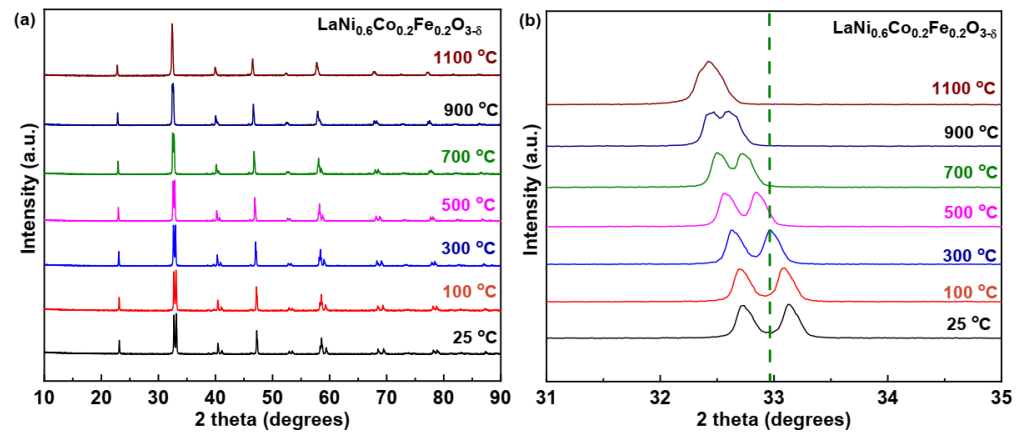


**Figure 4.** (**a**) Thermodiffraction patterns for $LaNi_{0.6}Co_{0.2}Fe_{0.2}O_{3-\delta}$ in the air from room temperature to 1100 °C. (**b**) Magnified XRD patterns in the 2-theta range of 31–35 showing the shift in peaks towards lower 2-theta degrees.

The effect of temperature on the lattice parameter (*a* and *c*) values for $LaNi_{0.6}Co_{0.2}Fe_{0.2}O_{3-\delta}$ in air is shown in Figure 5. Here, $\alpha_{ap-av.}$ is the average apparent thermal expansion coefficient value, caused by both chemically and thermally induced lattice changes, as explained before. The $ap - av$ TEC value of $LaNi_{0.6}Co_{0.2}Fe_{0.2}O_{3-\delta}$ is $14.98 \times 10^{-6}$ $K^{-1}$, which lies in the range of TEC values for $LaNi_{0.6}Co_{0.4}O_{3-\delta}$ from the literature ($14.6$–$17.5 \times 10^{-6}$ $K^{-1}$) [7,27,28].
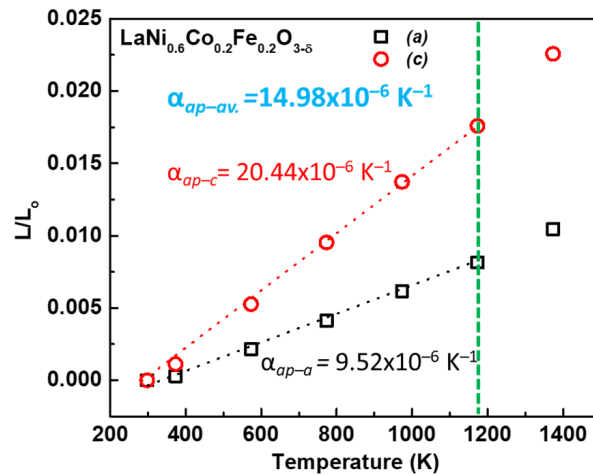


**Figure 5.** Lattice thermal expansion as a function of temperature for $LaNi_{0.6}Co_{0.2}Fe_{0.2}O_{3-\delta}$ in air ranging from room temperature to 1100 °C.

Figure 6 shows the temperature dependence of the electrical conductivity values of $LaNi_{0.6}Co_{0.4-x}Fe_xO_{3-\delta}$ (x = 0, 0.1, 0.2) in air. $LaNi_{0.6}Co_{0.4}O_{3-\delta}$ exhibits metallic-like conductivity, whereby the majority of the charge carriers are carried by the narrow itinerant conduction band of the Ni arrays (overlapping of *3d* Ni–*3d* Ni and *3d* Ni–*2p* O orbitals) [40]. Additionally, the contribution from *3d* Co is also possible in $LaNi_{0.6}Co_{0.4}O_{3-\delta}$, while in Fe-doped compositions, *3d* Co and *3d* Fe orbitals can also contribute to conduction band formation [40]. $LaNi_{0.6}Co_{0.3}Fe_{0.1}O_{3-\delta}$ (x = 0.1) showed the highest conductivity value of 697 S·cm$^{-1}$ at 800 °C, even higher than the $LaNi_{0.6}Co_{0.4}O_{3-\delta}$ phase. Further, an increase in Fe doping level to 0.2 led to a decrease in electrical conductivity values to 395 S·cm$^{-1}$ at 800 °C due to the decrease in the concentration of *p*-type charge carriers. The formation of oxide ion vacancies at higher temperatures resulted in reduction of the Fe and Co ions

($Fe^{4+}$ to $Fe^{3+}$ or $Co^{4+}$ to $Co^{3+}$), which in turn resulted in decreases in the *p*-type charge carrier concentration and the covalency of the (Co–Fe)–O bond [41,42]. For the Fe-doped samples with the increase in temperature, the conductivity first increased up to a maximum and then decreased due to the lattice oxygen loss (Equation (2)), indicating semiconductor behavior. This suggests that Fe doping leads to increased formation of oxygen vacancies. As has been shown in the literature, temperatures greater than 1000 °C are needed to create oxygen vacancies and introduce oxide ion conductivity in $LaNi_{0.6}Co_{0.4}O_{3-\delta}$ [43].



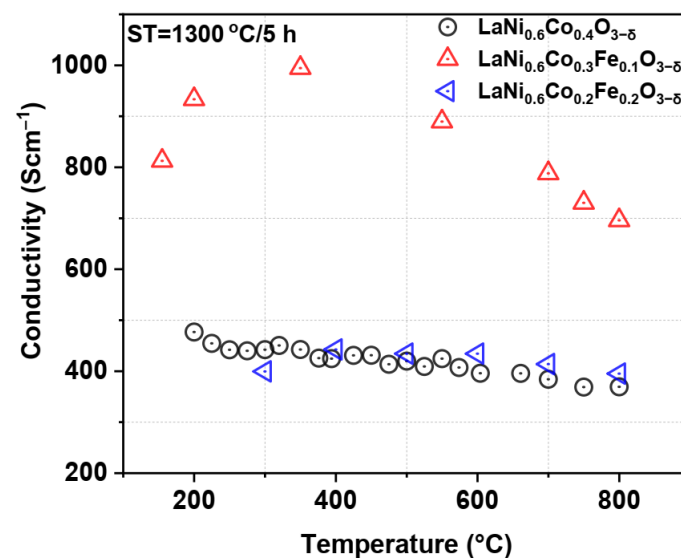**Figure 6.** Temperature dependence of electrical conductivity values for $LaNi_{0.6}Co_{0.4-x}Fe_xO_{3-\delta}$ (x = 0, 0.1, 0.2) in air.

## 4. Conclusions

$LaNi_{0.6}Co_{0.4-x}Fe_xO_{3-\delta}$ (x = 0–0.3) oxides were screened for electrical conductivity, TEC, and chemical compatibility with LCFCr and Crofer 22 APU interconnects to find an optimized contact material for RSOFCs. All of the proposed compositions were synthesized through the combustion method and single-phase powders were obtained for $LaNi_{0.6}Co_{0.3}Fe_{0.1}O_{3-\delta}$ and $LaNi_{0.6}Co_{0.2}Fe_{0.2}O_{3-\delta}$. The preparation of the composition with the highest doping of Fe (x = 0.3) showed $Fe_3O_4$ as a secondary phase, indicating that it is not possible to increase the amount of iron in the sample; hence, this composition was not further investigated. $LaNi_{0.6}Co_{0.3}Fe_{0.1}O_{3-\delta}$ showed the highest electrical conductivity value of 697 S·cm$^{-1}$ at 800 °C, while a further increase in the Fe amount (x = 0.2) decreased the value to 395 S·cm$^{-1}$ at 800 °C due to the decrease in the concentration of p-type charge carriers.

$LaNi_{0.6}Co_{0.2}Fe_{0.2}O_{3-\delta}$ was chosen as the best candidate owing to its acceptable TEC value of 14.98 × 10$^{-6}$ K$^{-1}$ from RT to 900 °C and electrical conductivity value of 395 S·cm$^{-1}$ at 800 °C. A structural transition from the rhombohedral phase to orthorhombic phase at temperatures greater than 900 °C was seen in thermodiffraction patterns for $LaNi_{0.6}Co_{0.2}Fe_{0.2}O_{3-\delta}$. Even though $LaNi_{0.6}Co_{0.3}Fe_{0.1}O_{3-\delta}$ exhibited higher electrical conductivity values, its TEC value was expected to be high due to the high Co content.

**Author Contributions:** Conceptualization, K.S., B.M.-S., P.K.A. and J.P.-G.; methodology, K.S., B.M.-S., P.K.A., V.T. and J.P.-G.; validation, K.S.; formal analysis, K.S.; investigation, K.S.; resources, V.T., B.M.-S., P.K.A. and J.P-G., data curation, K.S.; writing—original draft preparation, K.S.; writing—K.S., B.M.-S., P.K.A. and J.P.-G.; project administration, B.M.-S. and P.K.A.; funding acquisition, K.S., B.M.-S., P.K.A. and J.P-G. All authors have read and agreed to the published version of the manuscript.

# References

1. Mogensen, M.B.; Chen, M.; Frandsen, H.L.; Graves, C.; Hansen, J.B.; Hansen, K.V.; Hauch, A.; Jacobsen, T.; Jensen, S.H.; Skafte, T.L.; et al. Reversible solid-oxide cells for clean and sustainable energy. *Clean Energy* **2019**, *3*, 175–201. [CrossRef]

2. Kwon, Y.; Kang, S.; Bae, J. Development of a $PrBaMn_2O_{5+\delta}$-$La_{0.8}Sr_{0.2}Ga_{0.85}Mg_{0.15}O_{3-\delta}$ composite electrode by scaffold infiltration for reversible solid oxide fuel cell applications. *Int. J. Hydrog. Energy* **2020**, *45*, 1748–1758. [CrossRef]

3. Mogensen, M.B. Materials for reversible solid oxide cells. *Curr. Opin. Electrochem.* **2020**, *21*, 265–273. [CrossRef]

4. Shen, M.; Ai, F.; Ma, H.; Xu, H.; Zhang, Y. Progress and prospects of reversible solid oxide fuel cell materials. *iScience* **2021**, *24*, 103464. [CrossRef]

5. Simner, S.P.; Anderson, M.D.; Pederson, L.R.; Stevenson, J.W. Performance variability of $La(Sr)FeO_3$ SOFC cathode with Pt, Ag and Au current collectors. *J. Electrochem. Soc.* **2005**, *152*, A1851–A1859. [CrossRef]

6. Mori, M.; Liu, Y. $La_{0.6}Sr_{0.4}Co_{0.2}Fe_{0.8}O_{3-\delta}$ current collectors via Ag infiltration for microtubular solid oxide fuel cells with intermediate temperature operation. *J. Electrochem. Soc.* **2009**, *156*, B1182–B1187. [CrossRef]

7. Tucker, M.C.; Cheng, L.; DeJonghe, L.C. Selection of cathode contact materials for solid oxide fuel cells. *J. Power Sources* **2011**, *196*, 8313–8322. [CrossRef]

8. Morán-Ruiz, A.; Vidal, K.; Larrañaga, A.; Arriortua, M.I. Chemical compatibility and electrical contact of $LaNi_{0.6}Co_{0.4}O_{3-\delta}$ (LNC) between Crofer22APU interconnect and $La_{0.6}Sr_{0.4}FeO_3$ (LSF) cathode for IT-SOFC. *Fuel Cells* **2013**, *13*, 398–403. [CrossRef]

9. Wilkinson, L.T.; Zhu, J.H. Ag-Perovskite composite materials for SOFC cathode–interconnect contact. *J. Electrochem. Soc.* **2009**, *156*, B905–B912. [CrossRef]

10. Yang, Z.; Xia, G.; Singh, P.; Stevenson, J.W. Electrical contacts between cathodes and metallic interconnects in solid oxide fuel cells. *J. Power Sources* **2006**, *155*, 246–252. [CrossRef]

11. Stodolny, M.K.; Boukamp, A.B.; Blank, D.H.A.; Van Berkel, F.P.F. $La(Ni,Fe)O_3$ stability in the presence of chromia—A solid-state reactivity study. *J. Electrochem. Soc.* **2011**, *158*, B112–B116. [CrossRef]

12. Sharma, V.I.; Yildiz, B. Degradation mechanism in $La_{0.8}Sr_{0.2}CoO_3$ as contact layer on the solid oxide electrolysis cell anode. *J. Electrochem. Soc.* **2010**, *157*, B441–B448. [CrossRef]

13. Kim, S.J.; Kim, K.J.; Choi, G.M. Effect of $Ce_{0.43}Zr_{0.43}Gd_{0.1}Y_{0.04}O_{2-\delta}$ contact layer on the stability of the interface between GDC interlayer and YSZ electrolyte in the solid oxide electrolysis cell. *J. Power Sources* **2015**, *284*, 617–622. [CrossRef]

14. Molero Sánchez, B. Development of Oxygen Electrodes for Reversible Solid Oxide Fuel Cells. Ph.D. Thesis, University of Calgary, Calgary, AB, Canada, 2017.

15. Molero Sánchez, B.; Addo, P.; Buyukaksoy, A.; Birss, V. Performance enhancement of $La_{0.3}Ca_{0.7}Fe_{0.7}Cr_{0.3}O_{3-\delta}$ air electrodes by infiltration methods. *J. Electrochem. Soc.* **2017**, *164*, F3123–F3130. [CrossRef]

16. Quick Info. 2021. Available online: http://seeo2energy.com/ (accessed on 8 December 2021).

17. Molero Sánchez, B.; Prado-Gonjal, J.; Ávila-Brande, D.; Chen, M.; Morán, E.; Birss, V. High performance $La_{0.3}Ca_{0.7}Cr_{0.3}Fe_{0.7}O_{3-\delta}$ air electrode for reversible solid oxide fuel cell applications. *Int. J. Hydrog. Energy* **2015**, *40*, 1902–1910. [CrossRef]

18. Molero Sánchez, B.; Prado-Gonjal, J.; Ávila-Brande, D.; Chen, M.; Morán, E.; Birss, V. Microwave-assisted synthesis and characterization of new cathodic material for solid oxide fuel cells: $La_{0.3}Ca_{0.7}Fe_{0.7}Cr_{0.3}O_{3-\delta}$. *Ceram. Int.* **2015**, *41*, 8411–8416. [CrossRef]

19. Addo, P.K.; Molero Sánchez, B.; Chen, M.; Paulson, S.; Birss, V. $CO/CO_2$ study of high performance $La_{0.3}Sr_{0.7}Fe_{0.7}Cr_{0.3}O_{3-\delta}$ reversible SOFC electrodes. *Fuel Cells* **2015**, *15*, 689–696. [CrossRef]

20. Molero Sánchez, B.; Addo, P.K.; Buyukaksoy, A.; Paulson, S.; Birss, V. Electrochemistry of $La_{0.3}Sr_{0.7}Fe_{0.7}Cr_{0.3}O_{3-\delta}$ as an oxygen and fuel electrode for RSOFCs. *Faraday Discuss.* **2015**, *182*, 159–175. [CrossRef]

21. Addo, P.K.; Molero Sánchez, B.; Buyukaksoy, A.; Paulson, S.; Birss, V. Sulfur tolerance of $La_{0.3}M_{0.7}Fe_{0.7}Cr_{0.3}O_{3-\delta}$ (M = Sr, Ca) solid oxide fuel cell anodes. *ECS Trans.* **2015**, *66*, 219. [CrossRef]

22. Masood Ansari, H.; Stuart, B.A.; Ahmad, N.; Birss, V. Unraveling the evolution of exsolved Fe–Ni alloy nanoparticles in Ni-doped $La_{0.3}Ca_{0.7}Fe_{0.7}Cr_{0.3}O_{3-\delta}$ and their role in enhancing $CO_2$–CO electrocatalysis. *J. Mater. Chem. A* **2021**. [CrossRef]

23. Zhu, J.H.; Ghezel-Ayagh, H. Cathode-side electrical contact and contact materials for solid oxide fuel cell stacking: A review. *Int. J. Hydrog. Energy* **2017**, *42*, 24278–24300. [CrossRef]

24. Shong, W.-J.; Liu, C.-K.; Yang, P.; Lee, R.-Y.; Lin, K.-F. Evaluation of Ag–NiO mixture as a cathode contact material for solid oxide fuel cell applications. *J. Ceram. Soc. Jpn.* **2017**, *125*, 202–207. [CrossRef]

25. Singh, P.; Yang, Z.; Viswanathan, V.; Stevenson, J.W. Observations on the structural degradation of silver during simultaneous exposure to oxidizing and reducing environments. *J. Mater. Eng. Perform.* **2004**, *13*, 287–294. [CrossRef]

26. Lu, Z.G.; Zhu, J.H. Thermal Evaporation of pure Ag in SOFC-relevant environments. *Electrochem. Solid State Lett.* **2007**, *10*, B179–B182. [CrossRef]

27. Morán-Ruiz, A.; Vidal, K.; Laguna-Bercero, M.Á.; Larrañaga, A.; Arriortua, M.I. Effects of using $(La_{0.8}Sr_{0.2})_{0.95}Fe_{0.6}Mn_{0.3}Co_{0.1}O_3$ (LSFMC), $LaNi_{0.6}Fe_{0.4}O_{3-\delta}$ (LNF) and $LaNi_{0.6}Co_{0.4}O_{3-\delta}$ (LNC) as contact materials on solid oxide fuel cells. *J. Power Sources* **2014**, *248*, 1067–1076. [CrossRef]

28. Budiman, R.A.; Uzumaki, Y.; Hong, H.J.; Miyazaki, T.; Hashimoto, S.; Nakamura, T.; Yashiro, K.; Amezawa, K.; Kawada, T. Oxygen nonstoichiometry and transport properties of $LaNi_{0.6}Co_{0.4}O_{3-\delta}$. *Solid State Ion.* **2016**, *292*, 52–58. [CrossRef]

29. Qiu, L.; Ichikawa, T.; Hirano, A.; Imanishi, N.; Takeda, Y. $Ln_{1-x}Sr_xCo_{1-y}Fe_yO_{3-\delta}$ (Ln = Pr, Nd, Gd; x = 0.2, 0.3) for the electrodes of solid oxide fuel cells. *Solid State Ion.* **2003**, *158*, 55–65. [CrossRef]

30. Zhao, L.; Shen, J.; He, B.; Chen, F.; Xia, C. Synthesis, characterization and evaluation of $PrBaCo_{2-x}Fe_xO_{5+\delta}$ as cathodes for intermediate-temperature solid oxide fuel cells. *Int. J. Hydrog. Energy* **2011**, *36*, 3658–3665. [CrossRef]

31. Choi, S.; Yoo, S.; Kim, J.; Park, S.; Jun, A.; Sengodan, S.; Kim, J.; Shin, J.; Jeong-Young, H.; Choi-Man, Y.; et al. Highly efficient and robust cathode materials for low-temperature solid oxide fuel cells: $PrBa_{0.5}Sr_{0.5}Co_{2-x}Fe_xO_{5+\delta}$. *Sci. Rep.* **2013**, *3*, 2426. [CrossRef]

32. Ullmann, H.; Trofimenko, N.; Tietz, F.; Stover, D.; Ahmad-Khanlou, A. Correlation between thermal expansion and oxide ion transport in mixed conducting perovskite-type oxides for SOFC cathodes. *Solid State Ion.* **2000**, *138*, 79–90. [CrossRef]

33. Huczkowski, P.; Christiansen, N.; Shemet, V.; Niewolak, L.; Abellan, J.; Singheiser, L.; Quadakkers, W.J. Growth mechanisms and electrical conductivity of oxide scales on ferritic steels proposed as interconnect materials for SOFC's. *Fuel Cells* **2006**, *6*, 93–99. [CrossRef]

34. Quadakkers, W.J.; Shemet, V.; Singheiser, L. High-Temperature Material. U.S. Patent No US6936217B2, 2003.

35. VDM®Crofer 22 APU. 2021. Available online: https://www.vdm-metals.com/fileadmin/user_upload/Downloads/Data_Sheets/Data_Sheet_VDM_Crofer_22_APU.pdf (accessed on 8 December 2021).

36. Shannon, R.D. Revised effective ionic radii and systematic studies of interatomic distances in halides and chalcogenides. *Acta Cryst.* **1976**, *32*, 751–767. [CrossRef]

37. Nagai, T.; Ito, W.; Sakon, T. Change in the thermal expansion of a perovskite-type mixed conductor upon sample density. *J. Am. Ceram. Soc.* **2008**, *91*, 303–307. [CrossRef]

38. Marrocchelli, D.; Bishop, R.S.; Tuller, H.L.; Yildiz, B. Understanding chemical expansion in non-stoichiometric oxides: Ceria and zirconia case studies. *Adv. Funct. Mater.* **2012**, *22*, 1958–1965. [CrossRef]

39. Sun, J.; Liu, X.; Han, F.; Zhu, L.; Bi, H.; Wang, H.; Yu, S.; Pei, L. $NdBa_{1-x}Co_2O_{5+\delta}$ as cathode materials for IT-SOFC. *Solid State Ion.* **2016**, *288*, 54–60. [CrossRef]

40. Huang, K.; Lee, H.Y.; Goodenough, J.B. Sr- and Ni-Doped $LaCoO_3$ and $LaFeO_3$ Perovskites. *J. Electrochem. Soc.* **1998**, *145*, 3220–3227. [CrossRef]

41. Takahashi, H.; Munakata, F.; Yamanaka, M. Ab initio study of the electronic structures in $LaCoO_3$–$SrCoO_3$ systems. *Phys. Rev. B* **1998**, *57*, 15211. [CrossRef]

42. Lee, K.T.; Manthiram, A. $LaSr_3Fe_{3-y}Co_yO_{10-\delta}$ ($0 \le y \le 1.5$) intergrowth oxide cathodes for intermediate tem-perature solid oxide fuel cells. *Chem. Mater.* **2006**, *18*, 1621–1626. [CrossRef]

43. Hjalmarsson, P.; Søgaard, M.; Hagen, A.; Mogensen, M. Structural properties and electrochemical performance of strontium- and nickel-substituted lanthanum cobaltite. *Solid State Ion.* **2008**, *179*, 636–646. [CrossRef]